Numerical Simulation of the Nonlinear Magnetic Quantum Response of a Torus

A Thesis

Presented in Partial Fulfillment of the Requirements for the

Degree of Master of Science

with a

Major in Electrical Engineering

in the

College of Graduate Studies

University of Idaho

by

Phillip Andrew Hagen

Major Professor: Dennis Sullivan, Ph.D.

Committee Members: Mark Kuzyk, Ph.D.; Ata Zadehgol, Ph.D.

Department Administrator: Joseph Law, Ph.D.

August 2021

Authorization to Submit Thesis

This thesis of Phillip Andrew Hagen, submitted for the degree of Master of Science with a Major in Electrical Engineering and titled "Numerical Simulation of the Nonlinear Magnetic Quantum Response of a Torus," has been reviewed in final form. Permission, as indicated by the signatures and dates below, is now granted to submit final copies to the College of Graduate Studies for approval.

Major Professor: _____ Date: _____
Dennis Sullivan, Ph.D.

Committee Members: _____ Date: _____
Mark Kuzyk, Ph.D.

_____ Date: _____
Ata Zadehgol, Ph.D.

Department
Administrator: _____ Date: _____
Joseph Law, Ph.D.

Abstract

The nonlinear-optical response of a material leads to novel phenomena and applications. At present, most nonlinear-optical materials are based on the electric susceptibility. This thesis investigates the magnetic susceptibility as an alternative that might lead to a greatly enhanced nonlinear-optical response. To assess the nonlinearity of test systems, the Schrödinger equation and magnetic dipole moment operator are coded in Python using the finite-difference time-domain (FDTD) method to calculate the eigenstates and eigenenergies of a three-dimensional (3D) toroidal potential well, which is chosen as a prototypical magnetic system. The numerical results compare favorably with the analytical solution of the Schrödinger equation for the special case of a quantum wire, thus validating the method. A calculation of the magnetic dipole moment as a function of magnetic field strength demonstrates a nonlinear magnetic response, suggesting that such materials might be candidates for the next generation of nonlinear-optical materials.

Acknowledgements

I would like to thank Dr. Dennis Sullivan for his immense amount of help and support on this project. Dr. Sullivan always found a way to explain any questions on the code or on the FDTD method. He always supported and encouraged my ideas, problem solving method, and learning techniques. He found a way to remain patient and keep me motivated to move forward even when I was seemingly at a dead-end. I am very grateful for the opportunity to study under and learn so much from Dr. Sullivan.

I would also like to thank Dr. Mark Kuzyk for the insight into the nonlinear optics and quantum mechanical aspects of this project. Dr. Kuzyk answered every question regarding the physics of the project in a manner that was easily understood. He was always able to provide guidance and clarification when necessary.

Dedication

I would not have been able to complete this project without the support from my family and friends. My parents have been encouraging and patient, offering countless words of support and advice as I continue my education.

I would also like to thank all the students I had the privilege of teaching during the pursuit of my Master's degree. Every class period and interaction I had with each of them reinforced the notion that I am on the right path in my goal to pursue a career in academia.

Finally, I would like to thank Dr. Ata Zadehgol for his support during my undergraduate and graduate education. Dr. Zadehgol always provides a smiling face and seemingly limitless enthusiasm. He sparked my passion for electrical engineering and always made the University of Idaho feel like home.

Table of Contents

List of Tables

List of Figures

Chapter 1: Introduction

This thesis describes computational methods that simulate the magnetic dipole moment of an electric charge confined to a torus with an externally-applied magnetic field. The goal is to determine the nonlinear susceptibility of the system, a quantity that is important for nonlinear-optical applications. The strength of an electrical dipole moment is limited to the linear distance that the charge is displaced. For a loop of fixed size, the current can, in principle, be made arbitrarily large. Therefore, we use computer simulations as the first step to exploring whether or not the magnetic susceptibility can exceed the electric ones. If so, a new area of research and application could follow.

The torus is the ideal system for this study because an applied magnetic field will change both the magnitude of the current and its average position within the tube. As the centroid of the orbiting current gets forced toward the inner tube wall, the induced magnetic dipole moment should become a nonlinear function of the applied magnetic field. This is analogous to the charge along a straight wire bunching up at its end in the presence of an applied electric field.

The central part of this thesis is the development of numerical techniques to calculate the wave function of an electric charge confined to a torus. Validation of the theory is made by comparing the limiting case of a small tube diameter with the exact solutions of the Schrödinger equation of a charge confined to a loop. The problem is then solved in the presence of a magnetic field to demonstrate that magnetic susceptibilities can be calculated.

The finite-difference time-domain (FDTD) method offers a numerical method capable of implementing the Schrödinger equation in a three-dimensional (3D) structure [1]. FDTD has been used to find eigenfunctions of arbitrarily shaped structures for use in computer simulation of quantum mechanical systems [2]. The FDTD method has also been used for the optical characterization of microcrystalline solar cells [3]. This work develops the FDTD method to calculate the wave function of a charge inside a torus allowing for differing tube radii and the addition of a magnetic field.

Python 3.8 is utilized to simulate the system using the FDTD method. Python is free, open-source, and well documented and widely used for scientific applications. The language offers most of the necessary packages like SciPy, NumPy, Matplotlib, and Pandas. Most of these packages are included in the Anaconda Distribution, which also includes Spyder, a cross-platform integrated development environment (IDE) optimized for use in scientific computing. Python is considered a top-level programming language that offers clean, tab-oriented, and easy-to-read syntax. Packages, like

Numba, allow Python speed-optimization by taking the Python code and compiling it into machine code to allow the NumPy arrays and loops to be executed with speeds that match low-level languages such as C++. Other considerations when implementing the FDTD method in Python are discussed in Appendix A.

1.1 Research Goal

The main goal of this research is to discover evidence of nonlinearities and determine the nonlinear susceptibility within the toroidal system by

1. Implementing the Schrödinger equation in Python using the FDTD method;

2. Simulating the wave function of an electric charge inside a 3D torus structure;

3. Calculating the eigenenergies of the first five excited states of the system;

4. Comparing simulation results to exact solutions of the Schrödinger equation;

5. Simulating the effects of a static magnetic field to illustrate the nonlinearity of the magnetic dipole moment of the system; and

6. Determining the induced magnetic dipole moment of each excited state as a function of magnetic field.

Chapter 2: The FDTD Method

The formulation in this chapter is drawn heavily from [4, 15]. The FDTD implementation begins with the time-dependent Schrödinger equation [5, 6], which is written in the following form:

$$\frac{\partial \psi(x,y,z,t)}{\partial t} = i\frac{\hbar}{2m_e}\left[\frac{\partial^2 \psi(x,y,z,t)}{\partial x^2} + \frac{\partial^2 \psi(x,y,z,t)}{\partial y^2} + \frac{\partial^2 \psi(x,y,z,t)}{\partial z^2}\right]$$
$$-\frac{i}{\hbar}V(x,y,z)\psi(x,y,z,t). \tag{1}$$

$\psi(x,y,z,t)$ is now separated into real and imaginary components:

$$\psi(x,y,z,t) = \psi_{real}(x,y,z,t) + i \cdot \psi_{imag}(x,y,z,t). \tag{2}$$

Substituting Eq. (2) into Eq. (1) leads to two coupled equations:

$$\frac{\partial \psi_{real}(x,y,z,t)}{\partial t} = -\frac{\hbar}{2m_e}\nabla^2\psi_{imag}(x,y,z,t) + \frac{1}{\hbar}V(x,y,z)\psi_{imag}(x,y,z,t), \tag{3a}$$

$$\frac{\partial \psi_{imag}(x,y,z,t)}{\partial t} = \frac{\hbar}{2m_e}\nabla^2\psi_{real}(x,y,z,t) - \frac{1}{\hbar}V(x,y,z)\psi_{real}(x,y,z,t). \tag{3b}$$

These equations need to be in a form that allows implementation in computer code. Taking the finite-difference approximations in space and time results in the following two coupled equations:

$$\psi_{real}^{k+1}(m,n,l) = \psi_{real}^{k}(m,n,l) + \frac{\Delta t}{\hbar}V(m,n,l)\psi_{imag}^{k+\frac{1}{2}}(m,n,l)$$
$$-\frac{\hbar}{2m_e}\frac{\Delta t}{(\Delta x)^2}\begin{bmatrix} \psi_{imag}^{k+\frac{1}{2}}(m+1,n,l) + \psi_{imag}^{k+\frac{1}{2}}(m-1,n,l) \\ +\psi_{imag}^{k+\frac{1}{2}}(m,n+1,l) + \psi_{imag}^{k+\frac{1}{2}}(m,n-1,l) \\ +\psi_{imag}^{k+\frac{1}{2}}(m,n,l+1) + \psi_{imag}^{k+\frac{1}{2}}(m,n,l-1) - 6\psi_{imag}^{k+\frac{1}{2}}(m,n,l) \end{bmatrix}, \tag{4a}$$

$$\psi_{imag}^{k+\frac{3}{2}}(m,n,l) = \psi_{imag}^{k+\frac{1}{2}}(m,n,l) - \frac{\Delta t}{\hbar}V(m,n,l)\psi_{real}^{k+1}(m,n,l)$$
$$+\frac{\hbar}{2m_e}\frac{\Delta t}{(\Delta x)^2}\begin{bmatrix} \psi_{real}^{k+1}(m+1,n,l) + \psi_{real}^{k+1}(m-1,n,l) \\ +\psi_{real}^{k+1}(m,n+1,l) + \psi_{real}^{k+1}(m,n-1,l) \\ +\psi_{real}^{k+1}(m,n,l+1) + \psi_{real}^{k+1}(m,n,l+1) - 6\psi_{real}^{k+1}(m,n,l) \end{bmatrix}. \tag{4b}$$

In Eq. (4) computational matrix positional integer indices *m, n, l* have replaced the Cartesian coordinates *x, y, z*, respectively, in Eq. (3). Similarly, the computational time step *k* has replaced *t*.

Once the cell size Δx is chosen, the time step Δt must also be chosen so the constants implementing the spatial Laplacian are small enough to maintain stability [7]. This alternate implementation of the real and imaginary components Eq. (4a) and (4b) simulates the behavior of the evolution of ψ in time. Details are available in the literature [6-15].

Figure 1 illustrates the quantum ring that will be used in the simulation. The ring is represented by a torus with a diameter of 70 Angstroms. The tube of the torus has a diameter of 12 Angstroms. The entire problem space is bordered by a perfectly matched layer (PML) [16, 17] that can absorb outgoing waves that would otherwise interfere with the simulation. The implementation has been described in a previous paper [11] and will not be repeated here. Figure 2 shows the XY- and YZ-planes of the FDTD problem space used for this problem including the potentials, monitoring point, and PML for the system. This figure is not to scale, but rather represents the shape of the system implemented in the FDTD code. The system is composed of 3D cells that are one Angstrom cubed in volume making up a 100 x 100 x 30 grid. Figure 3 shows the system implemented in Python with the torus shape at 0 eV and the rest of the system at 4.6 eV potential. The PML cannot be seen in Fig 1. The energies in both Figs. 2 and 3 represent the depth of the potential well at any point.
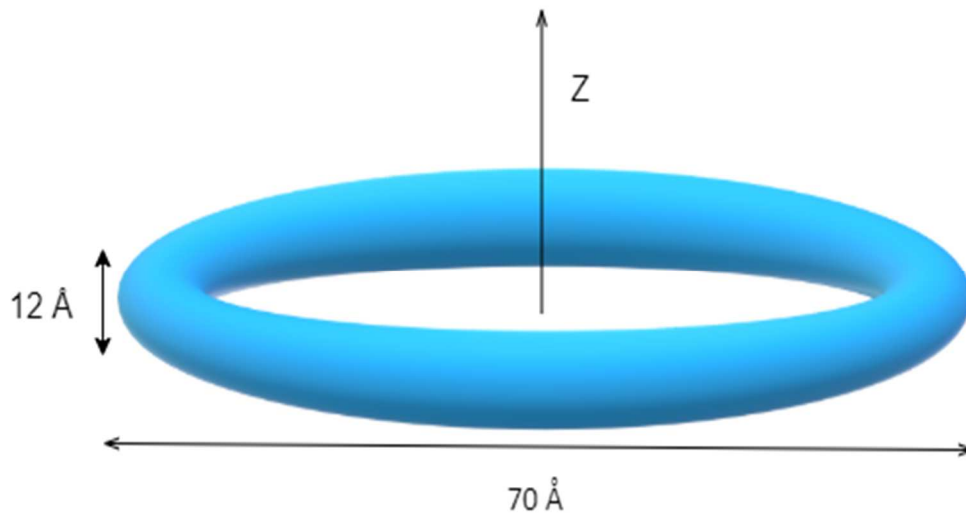
Figure 1. A quantum torus that is 70 Angstroms in diameter; the tube is 12 Angstroms in diameter.
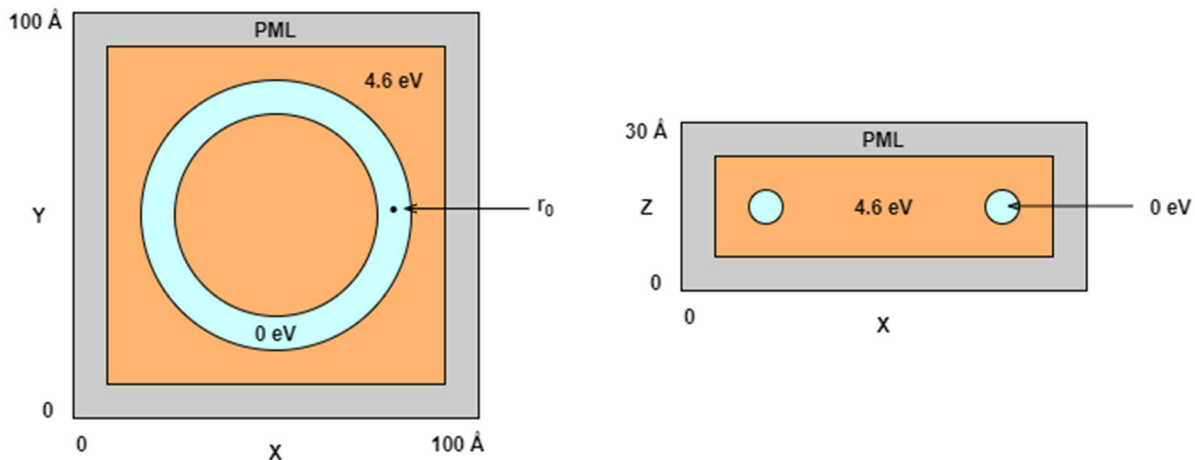
Figure 2. XY- and XZ-planes of the problem space containing the torus. The total problem space is 100 x 100 x 30 cells. Each cell is one Angstrom cubed. The energies represent the depth of the potential well in the given area.
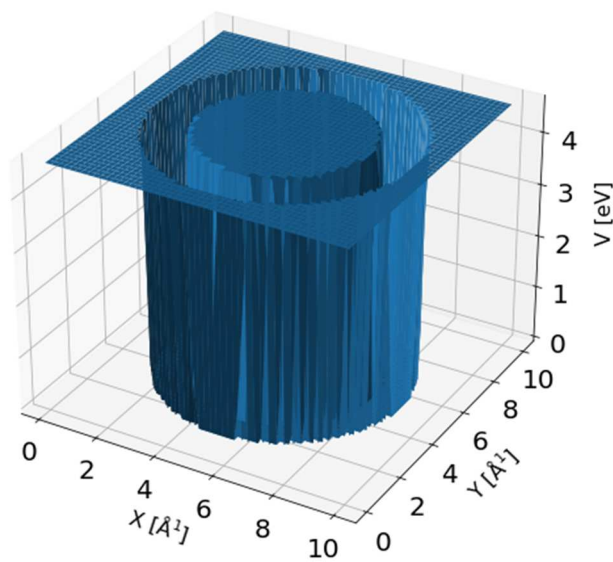
Figure 3. 3D view of a torus shaped potential well of 0 eV potential in a system of background potential 4.6 eV.

Chapter 3: Simulation of the Torus

3.1 Determining the Eigenstates of the Torus

The FDTD method can be used to determine the eigenenergy and eigenstates of a potential that may not have an analytic solution [18, 19]. Any quantum wave function in a quantum mechanical system can be written as a superposition of eigenstates,

$$\psi(r,t) = \sum_{n=0}^{N} \phi_n(r) e^{-i\left(\frac{\varepsilon_n}{\hbar}\right)t},$$ (5)

where $\phi_n(r)$ are the eigenfunctions of the system and the ε_n are their corresponding eigenenergies. The state variable, $\psi(r,t)$, can be written this way even if the eigenfunctions and eigenenergies are unknown. Calculating the eigenenergies of the system is accomplished by monitoring the time-domain data at one point in the torus, r_0, and then taking the Fourier transform:

$$F\{\psi(r_0,t)\} = \int_{-\infty}^{\infty} dt \left[\sum_{n=0}^{N} \phi_n(r_0) e^{-i\left(\frac{\varepsilon_n}{\hbar}\right)t}\right] e^{i\omega t} = \sum_{n=0}^{N} \phi_n(r_0) \delta\left(\omega - \frac{\varepsilon_n}{\hbar}\right).$$ (6)

The last step results from the orthogonality of the eigenfunctions:

$$\int_{-\infty}^{\infty} e^{-i(\omega_n - \omega_m)t} dt = \begin{cases} 1 & n = m \\ 0 & n \neq m \end{cases}.$$ (7)

The Fourier transform in Eq. (6) produces a series of Dirac-delta functions in the frequency domain corresponding to the eigenenergies of the system.

Usually, a narrow pulse that contains the eigenstates of the system is used as the initial wave function $\psi(r,t)$, in Eq. (5), as in [1]. However, to search for the ground state of the torus illustrated in Fig. 2, a test function that was radially symmetric within the torus was used to minimize the computational cost. Figure 4 shows this function. The FDTD simulation starts, and as time progresses, the time-domain data is saved at the point r_0 in the torus. Figure 5(a) shows the real component of the time-domain data at the monitoring point. Figure 5(b) shows the Fourier transform of this data and calculates the eigenenergy. The peak in Fig. 5(b) corresponds to the ground state energy of $\varepsilon_0 = 0.4646 \; eV$.
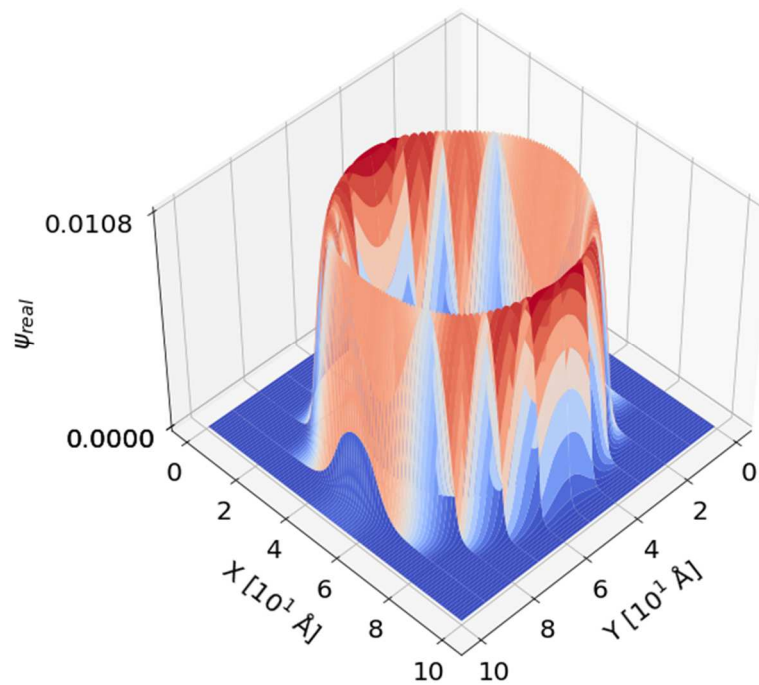
Figure 4. A narrow Gaussian pulse initialized within the torus.
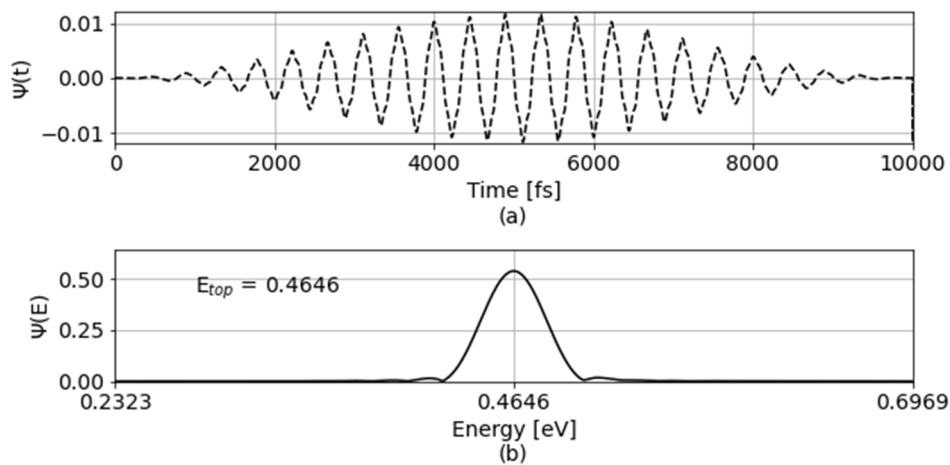
Figure 5. (a) The time-domain plot of the wavefunction at the monitoring point r_0;

(b) The Fourier transform of the time-domain data.

In order to determine the corresponding ground state eigenfunction $\phi_0(r)$, the discrete Fourier transform of the state variable is required at each point in the entire problem space for the frequency $\omega_0 = \frac{\varepsilon_0}{\hbar}$:

$$DFT\{\psi(r,t)\}_{\omega=\varepsilon_0/\hbar} = \int_{-\infty}^{\infty} dt \left[\sum_{n=0}^{N} \phi_n(r)e^{-i(\varepsilon_n/\hbar)t}\right]e^{i(\varepsilon_0/\hbar)t}$$

$$= \int_{-\infty}^{\infty} dt \left[\sum_{n=0}^{N} \phi_n(r)e^{-i((\varepsilon_n-\varepsilon_0)/\hbar)t}\right] = \phi_0(r). \tag{8}$$

Eq. (8) is implemented by a running Fourier Transform at each point in the problem space. This is described in detail in [2] and will not be repeated here. This calculation results in the waveform shown in Fig. 6.
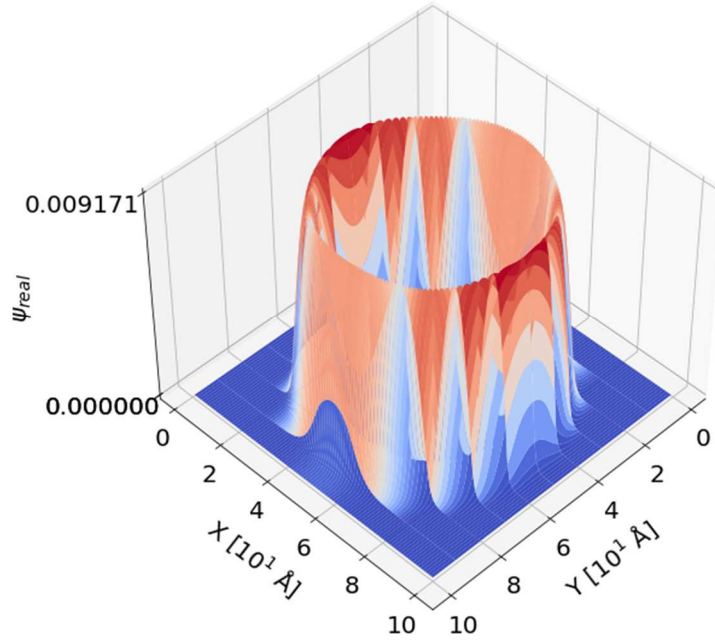
Figure 6. The ground state eigenfunction for a toroidal system with $r_{tube} = 6$ Å.

Higher order eigenstates can be generated by starting with the ground state eigenfunction of Fig. 6 and imposing the phase term $e^{i \cdot 2\pi \cdot n \cdot \theta}$, where n is the eigenfunction number. The wavefunction rotates counterclockwise as time progresses, illustrated by Fig. 7; the same is true of all the higher excited states. Eigenstates corresponding to negative integers rotate clockwise as time progresses. Figure 8 shows the wavefunction after 10,000 iterations for the ground state and each of the first five excited states, i.e., $n = 0, 1, 2, 3, 4, 5$. The system contains a ground state eigenenergy that can be found with

a Fourier transform. Each higher state also undergoes a Fourier transform at the monitoring point to determine the eigenenergy of that excited state. For comparison to the analytical solution of the Schrödinger equation for a quantum wire the simulated ground state eigenenergy is subtracted from the eigenenergy for each state calculated with Eq. (8).
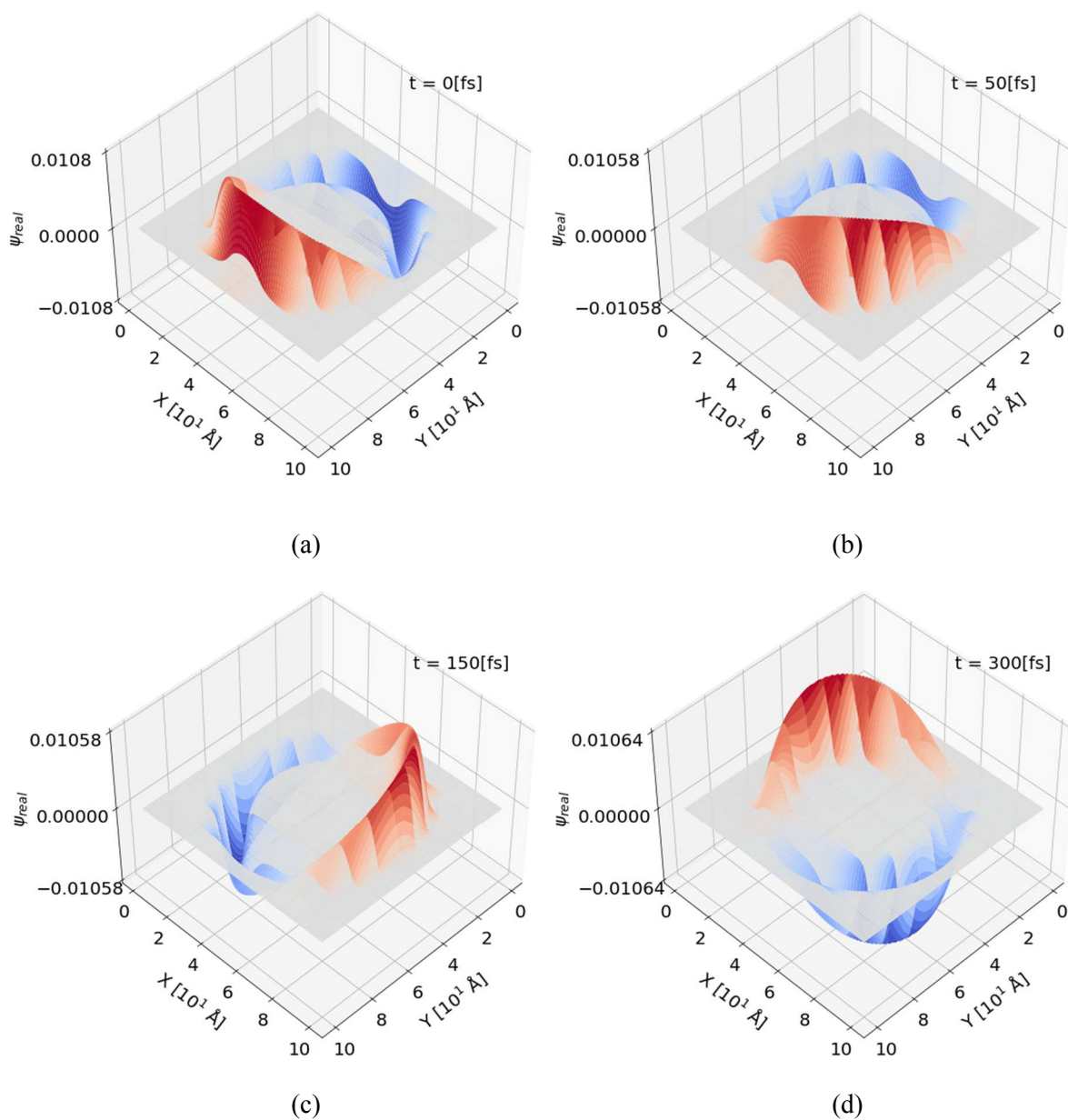
Figure 7. The real component of the wavefunction in the first excited state at (a) t = 0 fs; (b) t = 50 fs; (c) t = 150 fs; (d) t = 300 fs.
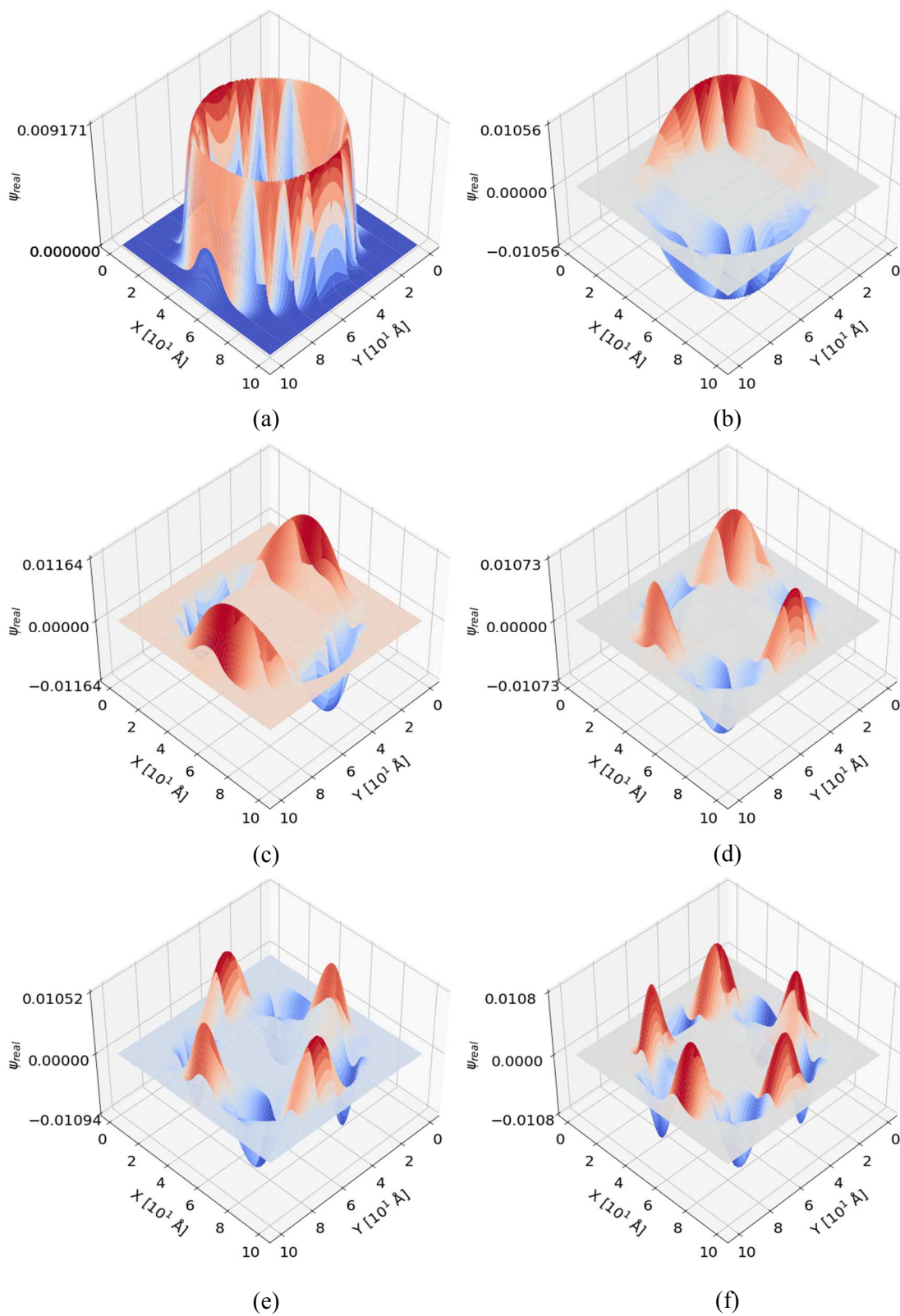
Figure 8. Real component of the wavefunction at the (a) Ground state; (b) First excited state; (c) Second excited state; (d) Third excited state; (e) Fourth excited state; (f) Fifth excited state.

3.2 Comparison with a Quantum Wire

The energies of the excited states can be determined by monitoring the waveforms in the torus at a single point and then taking the Fourier transform, as was done to determine the ground state energy in Fig. 5. The energies of the first five eigenstates are listed in Table 1.

The torus' eigenenergies are compared to those of the eigenstates of a quantum wire with the same diameter, as shown in Fig. 9(a). Due to the continuity of the wavefunction and the rotational symmetry of the loop, all eigenstates of the quantum wire must satisfy the periodic boundary condition, i.e., it must return to its original position after going around the circumference, as shown in Fig. 9(b). Therefore, any eigenenergy of the wire must have wavelengths of $2\pi \times 70$ angstroms divided by an integer. Therefore, the eigenenergies are:

$$KE_n = \frac{p_n^2}{2m} = \frac{1}{2m}\left(\frac{h}{\lambda_n}\right)^2 = \frac{1}{2m}\left(\frac{hn}{2\pi 70[\text{Å}]}\right)^2 \qquad (9)$$

These energies are also listed in Table 1.

In order to compare these values with those of the FDTD simulation, it is necessary to subtract the ground state energy from the FDTD calculated energies. This is done in Table 1 and Fig. 10.

Table 1. Analytical and Numerical eigenenergies for the first five excited states in a torus of $r_{tube} = 6$ Å.

State	Analytical (loop) ε [eV]	Numerical (torus) ε [eV]	Difference
1	0.003113	0.003308	6.3 %
2	0.012453	0.012198	2.0 %
3	0.028019	0.028325	1.1 %
4	0.049811	0.050034	0.45 %
5	0.07783	0.078152	0.41 %

(a)

(b)
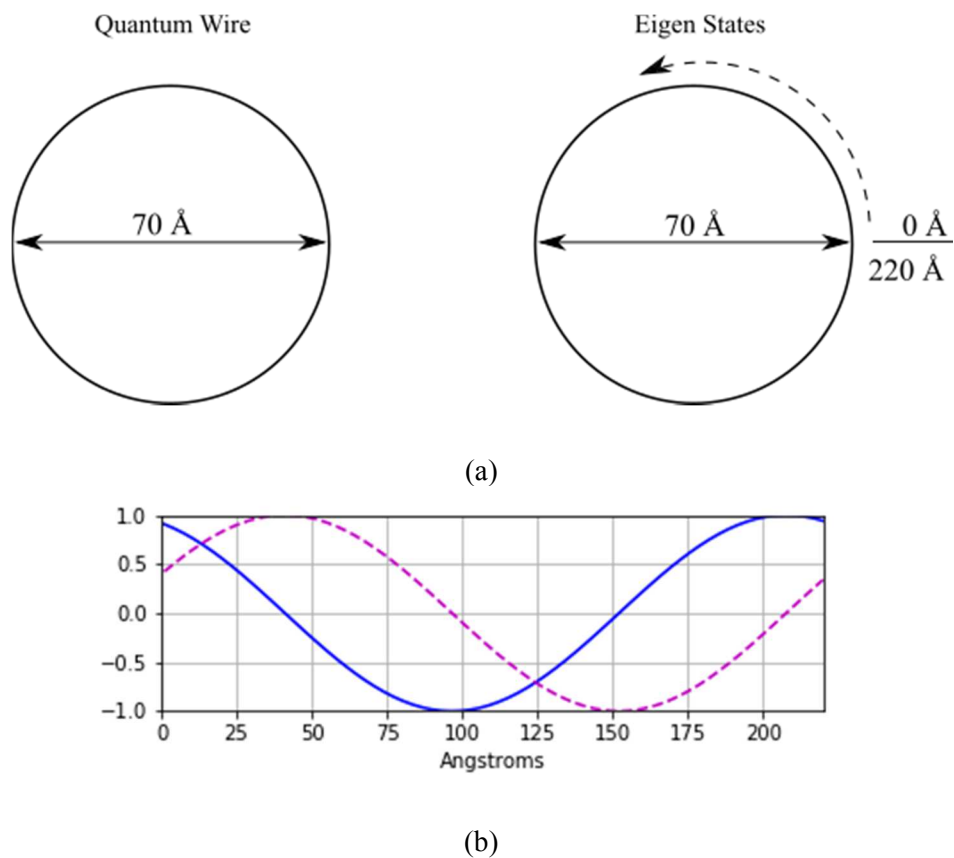
Figure 9. (a) Quantum wire with a loop diameter of 70 Å; (b) Monitoring of the real (blue) and imaginary (magenta) parts of the wavefunction as it travels around the circumference of the quantum wire.
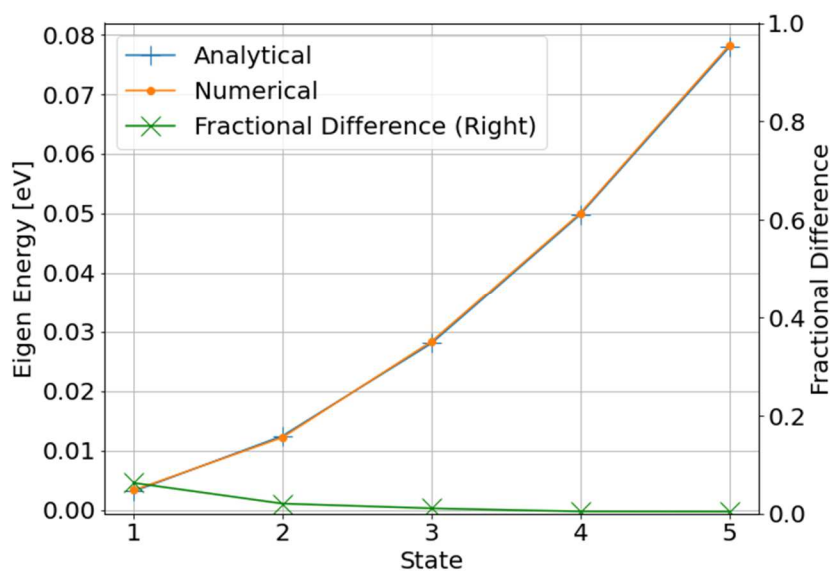
Figure 10. Comparison of the numerical and analytical eigenenergies for each excited state of an electric charge confined to a torus with $r_{tube} = 6$ Å.

3.3 Limiting the Size of the Tube Radius

The tube radius needs to be as small as possible within the simulation environment to be as close to the loop of quantum wire from Fig. 9(a) as possible. This quantum wire would have a tube radius of zero, which is not possible for the numerical method to calculate. The minimum tube radius for the simulation is one angstrom. Without an externally applied magnetic field, the charge will be on average in the center of the tube at any tube radius. The contour plots of the XY- and XZ-planes of the probability density after 10,000 iterations at a tube radius of six angstroms are illustrated by Fig. 11 that shows $|\psi|^2$, the probability density of the location of an electric charge within the torus. Figure 12 shows the probability density calculation after the same number of time steps for a tube radius of one angstrom. Each contour plot shows $|\psi|^2$ in the fifth excited state. All lower-energy states have similar results with the location of the centroid.

(a)   (b)
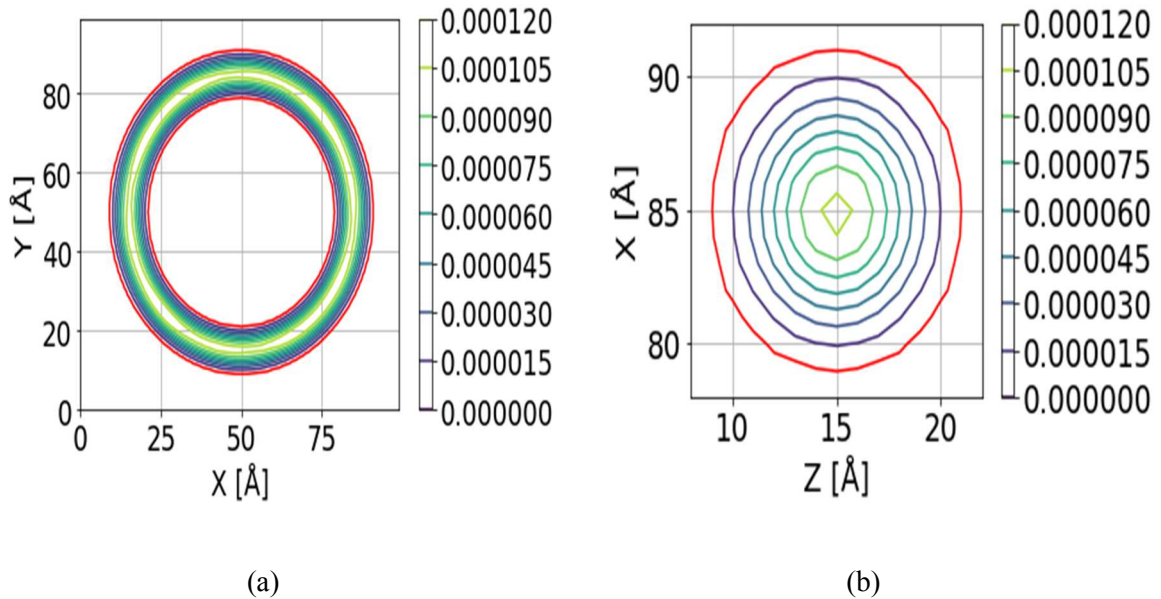
Figure 11. (a) XY-plane contour plot of the probability density, $|\psi|^2$, in the fifth excited state of the location of an electric charge confined in a torus (red) with $r_{tube} = 6$ Å confirming the location of the centroid is, on average, centered within the torus; (b) XZ-plane contour plot of the probability density, $|\psi|^2$, in the fifth excited state of the location of an electric charge confined in a torus (red) with $r_{tube} = 6$ Å confirming the location of the centroid is, on average, centered within the torus.
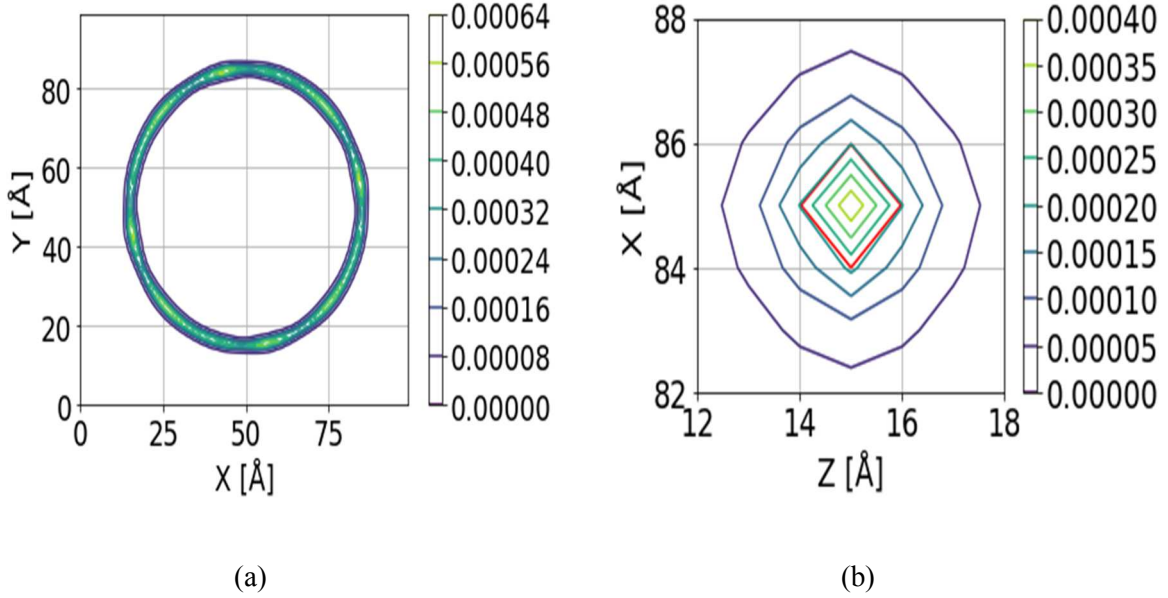
Figure 12. (a) XY-plane contour plot of the probability density, $|\psi|^2$, in the fifth excited state of the location of an electric charge confined in a torus (red) with $r_{tube} = 1$ Å confirming the location of the centroid is, on average, centered within the torus; (b) XZ-plane contour plot of the probability density, $|\psi|^2$, in the fifth excited state of the location of an electric charge confined in a torus (red) with $r_{tube} = 1$ Å confirming the location of the centroid is, on average, centered within the torus.

Figures 11 and 12 confirm the local maxima and minima are in the center of the torus in both the XY- and XZ- planes as the tube radius becomes small. The torus in the XZ- plane appears as a diamond shape at a tube radius of one angstrom because the FDTD cell size is one ,angstrom cubed. With only two FDTD cells for the entire diameter of the tube, it becomes impossible to model as a more circular shape. This problem could be solved by making the cell size smaller or by employing a sub-gridding algorithm [20, 21]. Either method would make the numerical method more accurate but would also cost valuable computational time. For this thesis, simulations ran in under two minutes, but still maintained accuracy to several significant digits. Comparisons of the eigenenergies at each excited state were made verifying the simulation method. Tables 2, 3, and 4 show the results follow a similar trend for tube radii of four, two, and one angstrom(s) and Figs. 13, 14, and 15 plot the comparisons of eigenenergies at tube radii of four, two, and one angstrom(s), respectively. The simulation method has the highest discrepancy during the second excited state where the radius of the tube is four angstroms at 10.3 percent difference between the analytical and numerical simulation result. All the eigenenergies were calculated using Fourier theory as described earlier in this thesis.

Table 2. Analytical and Numerical eigenenergies for the first five excited states of an electric charge in a torus of $r_{tube} = 4$ Å.

State	Analytical (loop) ε [eV]	Numerical (torus) ε [eV]	Difference
1	0.003113	0.003101	0.38 %
2	0.012453	0.011165	10.3 %
3	0.028019	0.028118	0.35 %
4	0.049811	0.05024	0.86 %
5	0.07783	0.076911	1.2 %

Table 3. Analytical and Numerical eigenenergies for the first five excited states in a torus of $r_{tube} = 2$ Å.

State	Analytical (loop) ε [eV]	Numerical (torus) ε [eV]	Difference
1	0.003113	0.003068	1.5 %
2	0.012453	0.011338	9.0 %
3	0.028019	0.02781	0.75 %
4	0.049811	0.049553	0.52 %
5	0.07783	0.07743	0.51 %

Table 4. Analytical and Numerical eigenenergies for the first five excited states in a torus of $r_{tube} = 1$ Å.

State	Analytical (loop) ε [eV]	Numerical (torus) ε [eV]	Difference
1	0.003113	0.003068	1.5 %
2	0.012453	0.011338	9.0 %
3	0.028019	0.026878	4.1 %
4	0.049811	0.051688	3.8 %
5	0.07783	0.076498	1.7 %

Figure 13. Comparison of the exact and simulated eigenenergies for each excited state inside a torus with $r_{tube} = 4$ Å.
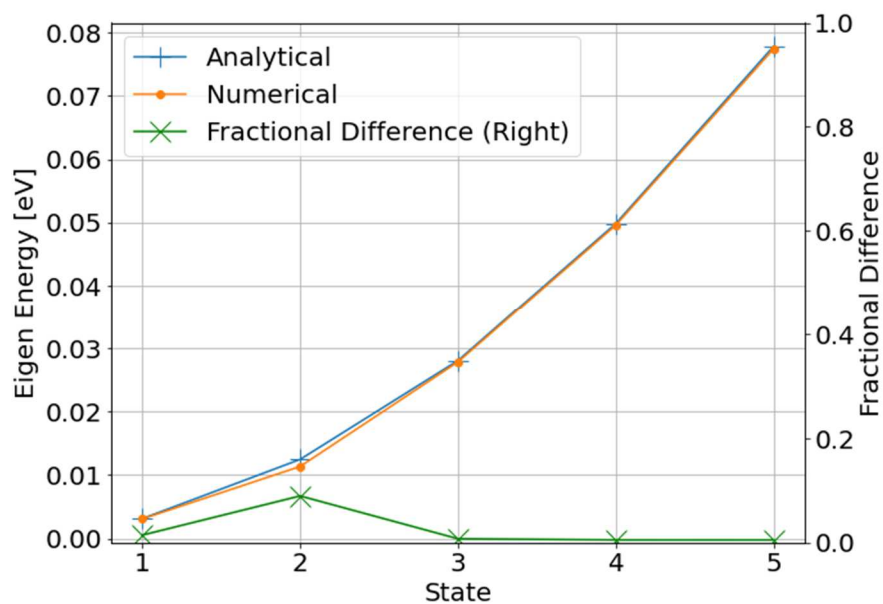
Figure 14. Comparison of the exact and simulated eigenenergies for each excited state inside a torus with $r_{tube} = 2$ Å.
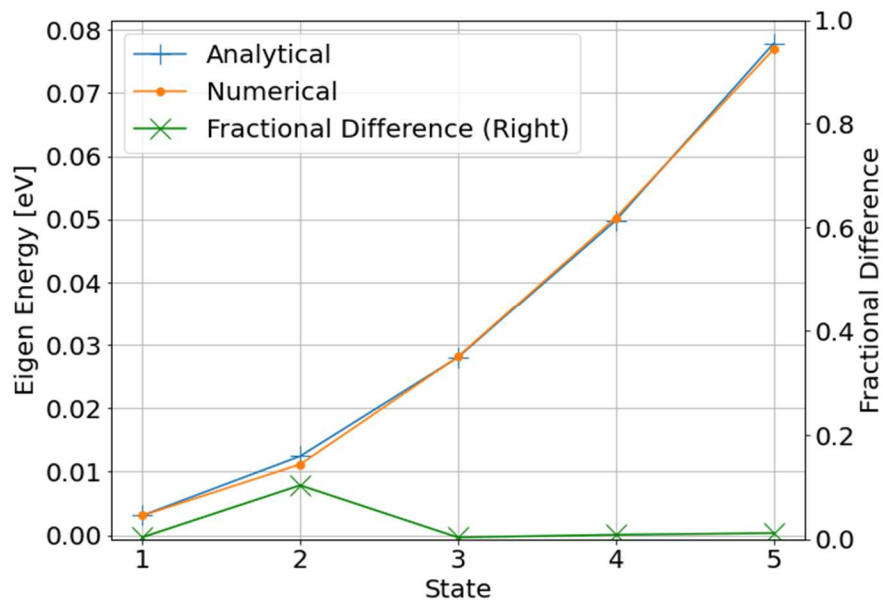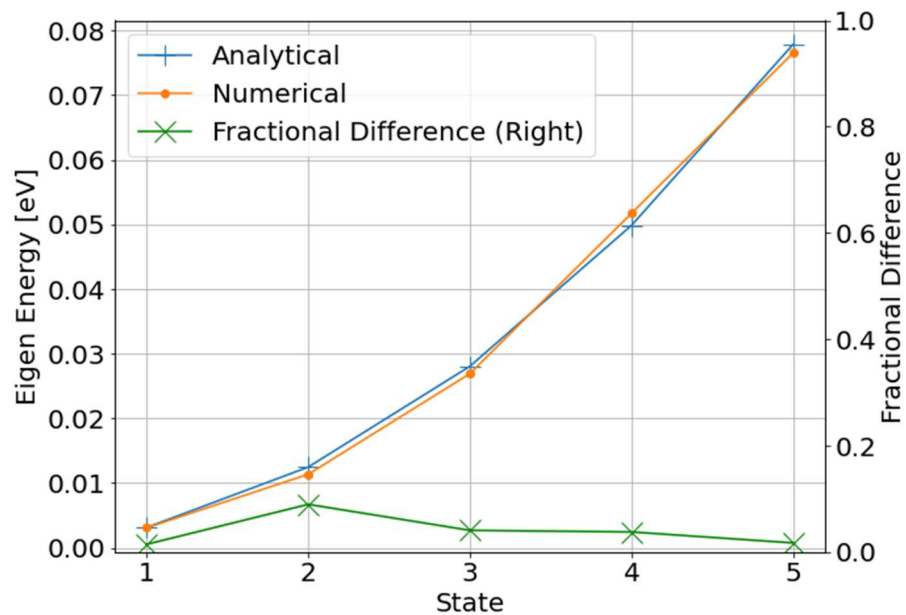
Figure 15. Comparison of the exact and simulated eigenenergies for each excited state inside a torus with $r_{tube} = 1$ Å.

Figures 13 through 15 find that the analytical eigenenergies of a particle in a wire loop converge to the numerical eigenenergies for the particle confined to a torus when at the higher energies at every tube radius.

Chapter 4: Calculation of the Magnetic Dipole Moment

The FDTD method can be used to solve the Schrödinger equation for the energy eigenfunctions and eigenenergies. This is done for an electric charge confined to a torus in the presence of an applied magnetic field, using the resulting wave function to calculate the induced magnetic dipole moment as a function of the applied magnetic field for each energy eigenfunction. This chapter uses that method to compare wave functions as a static magnetic field is applied and increases in intensity.

When a magnetic field is present, the Hamiltonian becomes:

$$H = \frac{1}{2m}\left(\frac{\hbar}{i}\nabla - q \cdot \boldsymbol{A}\right)^2 + V_{torus}(x,y,z). \tag{10}$$

This thesis restricts the magnetic field to the z-direction, so

$$\boldsymbol{B} = B_o\hat{\boldsymbol{z}}. \tag{11}$$

With this restriction $\boldsymbol{A}$ becomes:

$$\boldsymbol{A} = \frac{1}{2}(-yB_0\hat{\boldsymbol{x}} + xB_0\hat{\boldsymbol{y}}), \tag{12}$$

Making the Hamiltonian take the following form:

$$H = \frac{\hbar^2}{2m}\left(\frac{\partial^2}{\partial x^2} + \frac{\partial^2}{\partial y^2} + \frac{\partial^2}{\partial z^2}\right) + i\frac{\hbar B_0 q}{2m}\left(-y\frac{\partial}{\partial x} + x\frac{\partial}{\partial y}\right) + \frac{q^2 B_0^2}{8m}(x^2 + y^2) + V_{torus}(x,y,z). \tag{13}$$

This ignores the electric dipole interaction. The details of the implementation of Eq. (13) into FDTD have previously been described elsewhere [5, 6] and will not be reflected in this thesis. Figure 16 is a schematic representation of the system and an applied magnetic field.
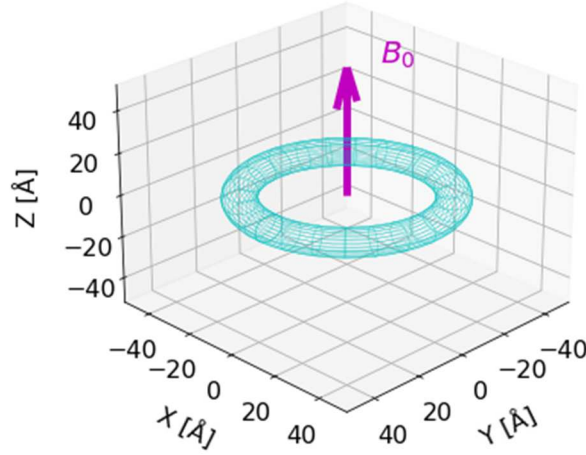
Figure 16. Torus system with an applied magnetic field.

The FDTD method formulated in Chapter 2 is implemented the same way, except Eq. (4) will now have a term accounting for the magnetic field.

$$
\begin{aligned}
\psi_{real}^{k+1}(m,n,l) = {}& \psi_{real}^{k}(m,n,l) + \frac{\Delta t}{\hbar} V(m,n,l)\psi_{imag}^{k+\frac{1}{2}}(m,n,l) \\
& -\frac{\hbar}{2m_e}\frac{\Delta t}{(\Delta x)^2}\left[\begin{array}{l} \psi_{imag}^{k+\frac{1}{2}}(m+1,n,l) + \psi_{imag}^{k+\frac{1}{2}}(m-1,n,l) \\ +\psi_{imag}^{k+\frac{1}{2}}(m,n+1,l) + \psi_{imag}^{k+\frac{1}{2}}(m,n-1,l) \\ +\psi_{imag}^{k+\frac{1}{2}}(m,n,l+1) + \psi_{imag}^{k+\frac{1}{2}}(m,n,l-1) - 6\psi_{imag}^{k+\frac{1}{2}}(m,n,l) \end{array}\right] \\
& +\frac{(\Delta t)(\Delta x)^2 q^2 B_0^2}{8m_e\hbar}[(m-X_c)^2 + (n-Y_c)^2]\,\psi_{imag}^{n+\frac{1}{2}}(m,n,l) \\
& +\frac{(\Delta t)qB_0}{4m_e}\left[\begin{array}{l} -(n-Y_c)\cdot[\psi_{real}^{n}(m+1,n,l) - \psi_{real}^{n}(m-1,n,l)] \\ +(m-X_c)\cdot[\psi_{real}^{n}(m,n+1,l) - \psi_{real}^{n}(m,n+1,l)] \end{array}\right],
\end{aligned}
\tag{14 a}
$$

$$
\begin{aligned}
\psi_{imag}^{k+\frac{3}{2}}(m,n,l) = {}& \psi_{imag}^{k+\frac{1}{2}}(m,n,l) + \frac{\Delta t}{\hbar} V(m,n,l)\psi_{real}^{k+1}(m,n,l) \\
& +\frac{\hbar}{2m_e}\frac{\Delta t}{(\Delta x)^2}\left[\begin{array}{l} \psi_{real}^{k+1}(m+1,n,l) + \psi_{real}^{k+1}(m-1,n,l) \\ +\psi_{real}^{k+1}(m,n+1,l) + \psi_{real}^{k+1}(m,n-1,l) \\ +\psi_{real}^{k+1}(m,n,l+1) + \psi_{real}^{k+1}(m,n,l-1) - 6\psi_{real}^{k+1}(m,n,l) \end{array}\right] \\
& -\frac{(\Delta t)(\Delta x)^2 q^2 B_0^2}{8m_e\hbar}[(m-X_c)^2 + (n-Y_c)^2]\,\psi_{real}^{k+1}(m,n,l) \\
& +\frac{(\Delta t)qB_0}{4m_e}\left[\begin{array}{l} -(n-Y_c)\cdot[\psi_{imag}^{k+\frac{1}{2}}(m+1,n,l) - \psi_{imag}^{k+\frac{1}{2}}(m-1,n,l)] \\ +(m-X_c)\cdot[\psi_{imag}^{k+\frac{1}{2}}(m,n+1,l) - \psi_{imag}^{k+\frac{1}{2}}(m,n+1,l)] \end{array}\right]
\end{aligned}
\tag{15 b}
$$

The $(m - X_c)$ and $(n - Y_c)$ terms replace x and y, respectively, since they are now measured from the center of the torus. X_c and Y_c represent the center point along the x- and y-axes, respectively. The center of the torus is symmetric about the z-axis, making $(m - X_c)$ and $(n - Y_c)$ the same value. The magnetic dipole moment operator needs to be calculated and implemented using the FDTD method. This process is detailed in the literature [1] and results in Eq. (16).

$$\boldsymbol{m} = -i\frac{q\hbar}{2m_e}\left[(x - X_c)\frac{\partial}{\partial y} - (y - Y_c)\frac{\partial}{\partial x}\right] - \frac{q^2 B(t)}{4m_e}[(x - X_c)^2 + (y - Y_c)^2] \tag{16}$$

The addition of a magnetic field to the quantum wire from Fig. 9(a) will speed up the current without changing the radius of the orbiting charge. Applying a static magnetic field to the torus changes the orbiting charge radius that will force the center of the wave function toward the inner wall of the torus instead of in the center of the torus as usual. The local maxima and minima of the wave function will also change as the strength of the magnetic field changes. Starting in the first excited state with no magnetic field and moving up to a field strength of 1000 T shows the difference in this behavior. Figure 17 shows the contour plot of the wave function of a torus with tube diameter of two angstroms without any applied magnetic field to establish a reference point for future comparisons. As expected, the wave function is, on average, centered inside the torus. As magnetic field strength increases this centroid will be forced toward the inner tube wall. The magnitude of the local maxima and minima will change as well. Table 5 shows the peak magnitudes of the wave function in the first excited state as magnetic field strength is increased toward a magnetic field of very high strength. The change in the wave function when a very large magnetic field is applied is about a 1.5 percent difference in maximum value. The minimum values have the same magnitude, but they are represented by a negative number.

These simulations are repeated for each state up to state five. The wave function is calculated using Eq, (13) for the ground state and the first five excited states of the system with an increasing magnetic field. The magnetic field increases in magnitude until $B_{amp} = 1000\ T$. The simulation iterates 10,000 time steps at this amplitude. The original wave function with no magnetic field is subtracted out of the wave function with the very high applied magnetic field. This difference in the probability density of the wave function without an applied magnetic field and the wave function when a static magnetic field of 1000 T is applied in the z-direction is illustrated in Figs. 18 through.21. The centroid of the orbiting current is no longer in the center of the torus structure and the peak magnitude has changed.

Table 5. Maximum values of the real component of ψ as a function of applied magnetic field for the wave function in the first eigenstate. As the magnetic field intensifies the value is compared to the value of ψ_{max} when no magnetic field is applied.

Magnetic Field [T]	ψ_{max}	Percent Change
0	0.021518	0.0 %
10	0.021521	0.01 %
100	0.021548	0.14 %
500	0.021672	0.72 %
1000	0.021823	1.42 %
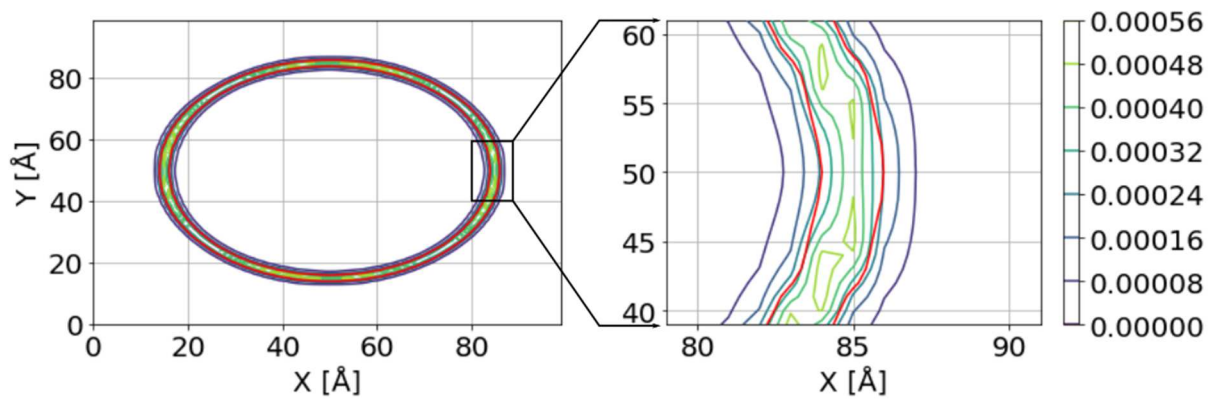
Figure 17. Contour plot of the probability density, $|\psi|^2$, of the location of an electric charge in the first excited state confined to a torus (red) of $r_{tube} = 1$ Å with no externally applied magnetic field.

Figure 18. Fractional change in the probability density, $|\psi|^2$, of the location of an electric charge in the first excited state between an applied magnetic field of 10 T and no applied magnetic field confined to a torus (red) of $r_{tube} = 1$ Å.

Figure 19. Fractional change in the probability density, $|\psi|^2$, of the location of an electric charge in the first excited state between an applied magnetic field of 100 T and no applied magnetic field confined to a torus (red) of $r_{tube} = 1$ Å.
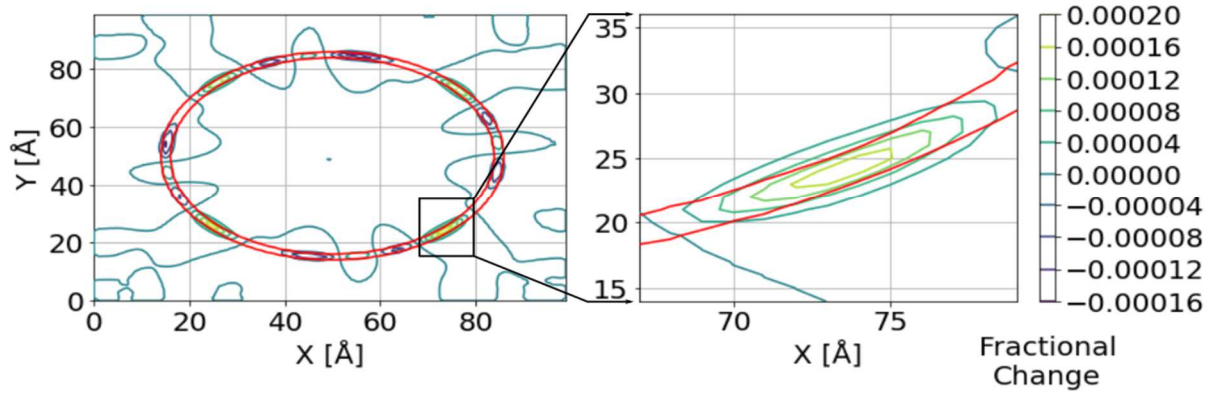
Figure 20. Fractional change in the probability density, $|\psi|^2$, of the location of an electric charge in the first excited state between an applied magnetic field of 500 T and no applied magnetic field confined to a torus (red) of $r_{tube} = 1$ Å.
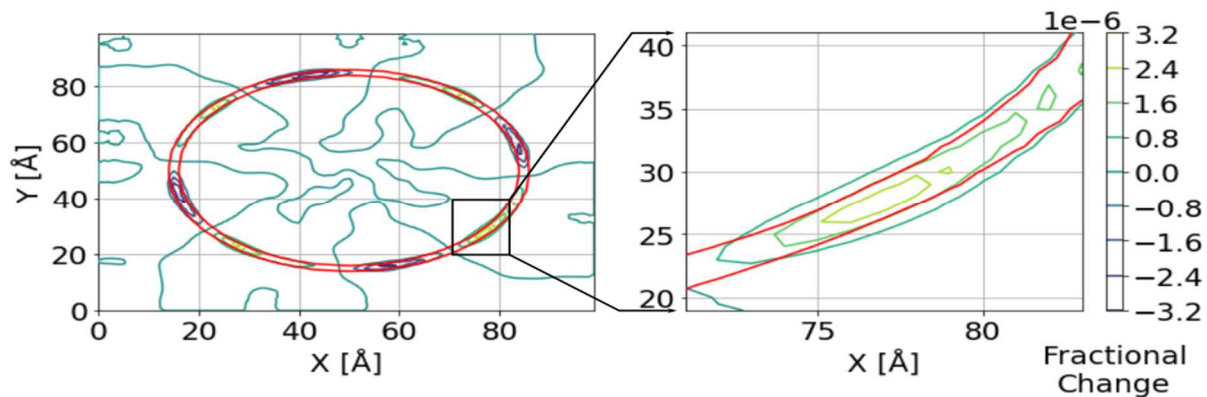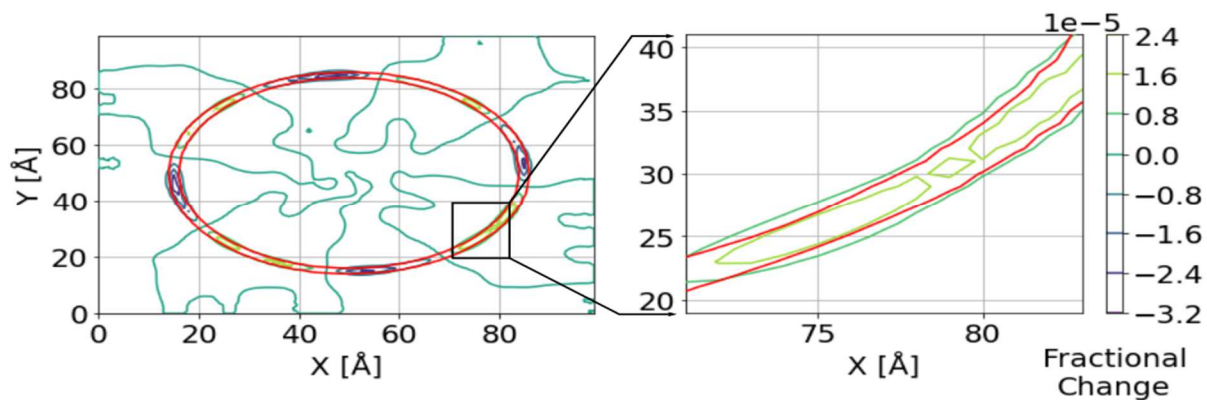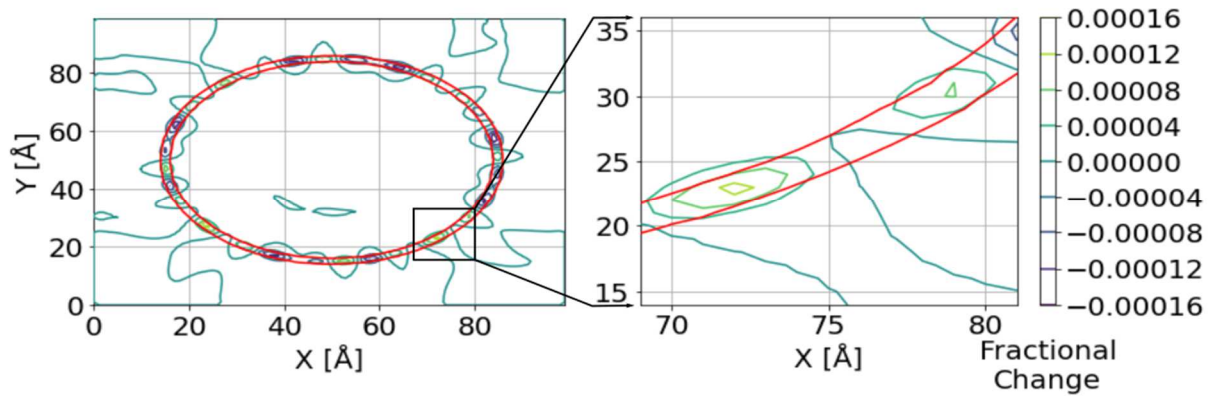

Figure 21. Fractional change in the probability density, $|\psi|^2$, of the location of an electric charge in the first excited state between an applied magnetic field of 1000 T and no applied magnetic field confined to a torus (red) of $r_{tube} = 1$ Å.

A magnetic field is applied in the positive z-direction and increased in magnitude. As this field increases, a dipole moment with an amplitude that increases nonlinearly is induced. This nonlinearly increasing amplitude is shown in Fig. 22. Furthermore, higher-energy states are observed to have a much larger nonlinearity. Figure 23 plots the magnetic dipole moment as a function of the magnetic field magnitude for each of the first five excited states showing the nonlinearity induced by the change in the radius of the orbiting charge. Each magnetic dipole moment is calculated using the FDTD method with 10,000 iterations. Figure 23 also proves the desired nonlinearity is created for each state as the magnitude of the magnetic field increases. This nonlinearity shows the charged

particles bunch up near the inner tube wall and may be used to optimize the non-linear optical response of the system.

The induced magnetic dipole moments are negative, so are in the opposite direction of the applied magnetic field, in accordance with Lenz's law (an induced electric current flows in a direction such that the current opposes the change that induced it). The induced magnetic dipole is a non-linear function of the amplitude of the applied magnetic field. Since the function is non-linear, the fractional change between the induced magnetic dipole moment with an applied field compared to the moment with no applied field is monitored.
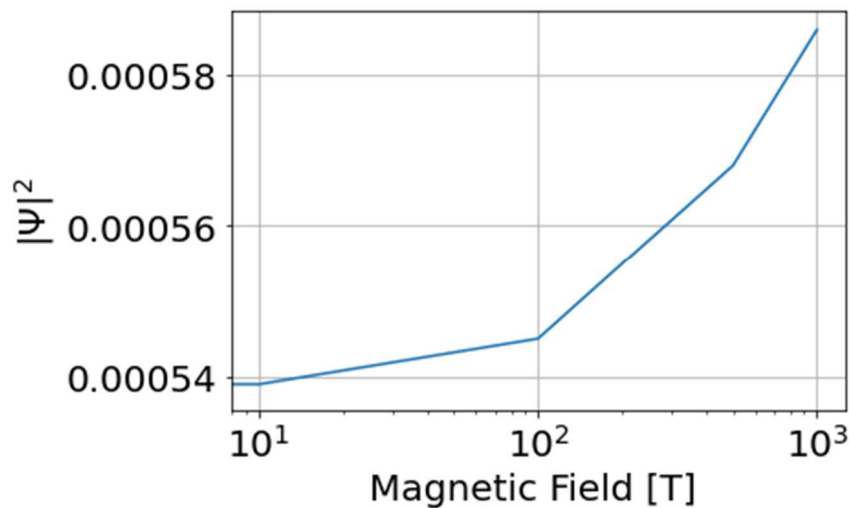
Figure 22. Nonlinear increase of the amplitude of $|\psi|^2$ as a function of magnetic field.

As the magnetic field increases in amplitude, the location of the peak amplitude changes. The orbiting charge increases speed and is forced toward the inner tube wall as the magnetic field strength increases. Recall from Fig. 9 in Chapter 3 the orbiting charge confined to the torus moves counterclockwise. Figure 24 shows the highest probable location of the peak amplitude of the charge. Fig. 24 illustrates that as the magnetic field increases the location of the peak increases in speed, i.e., moves further in the counterclockwise direction, and moves closer to the inner tube wall. The highest probable location of the charge is no longer in the center of the tube walls.

(a)

(b)

(c)

(d)

(e)
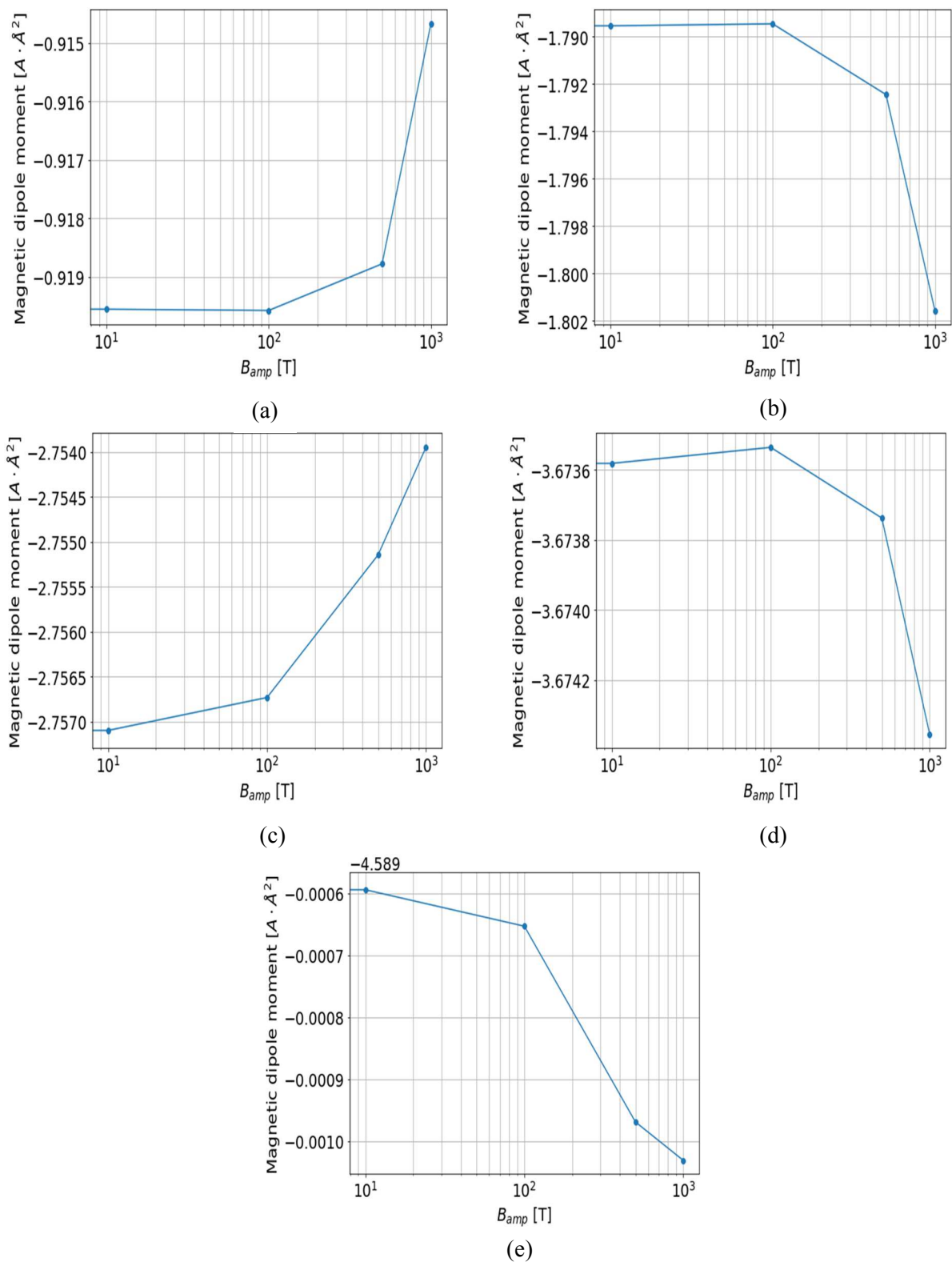
Figure 23. Magnetic dipole moment as a function of magnetic field strength for an electric charge confined to a torus with $r_{tube} = 6$ Å in the (a) first excited state; (b) second excited state; (c) third excited state; (d) fourth excited state; (e) fifth excited state.
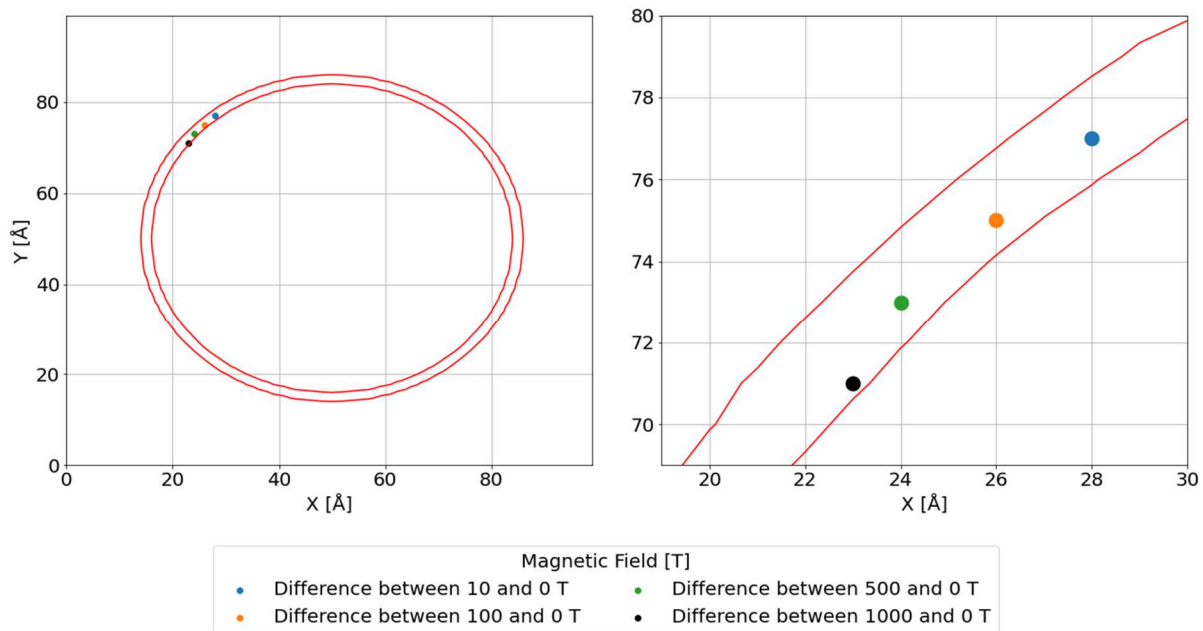
Figure 24. The change in peak amplitude location of $|\psi|^2$ of an electric charge confined to a torus (red) with $r_{tube} = 1$ Å. The peak of the wave function increases speed and is forced toward the inner tube wall.

Chapter 5: Conclusion

This thesis describes simulation methodology to determine nonlinear magnetic moments of an electric charge confined to a torus in the presence of a magnetic field. The core simulation method is the finite-difference time-domain method. FDTD provides a way to implement the Schrödinger equation for three-dimensional simulations. The structure chosen for this thesis was a torus with constant radius and varying tube diameters. The torus was chosen because in the absence of an applied magnetic field, the centroid of the current will be in the center of the tube. As a magnetic field is applied and increased in strength the centroid will get forced toward the inner tube wall, which results in a nonlinear dependence of the induced dipole moment on applied magnetic field.

The resolution of these simulations considers many factors such as cell size, problem space size, and the size of the time step. Any of these factors can be changed to adjust the resolution of the simulations but require the monitoring of certain parameters such as the shape of ψ_{real} and ψ_{imag} to make sure they do not become distorted or break down.

The real and imaginary components of the wave function were simulated for an electric charge inside a torus structure with a radius of 35 angstroms and a tube radius of sizes decreases from six to one angstrom(s) using an FDTD problem space consisting of one angstrom cubed cells constructing a 100x100x30 cell grid.

Exact numerical solutions to the Schrödinger equation were applied to the system. These values were compared to analytical values for a wire loop with the highest discrepancy of 10 percent occurring when the radius of the tube was four angstroms in the second state. These simulations used 10,000 iterations allowing for some error in the approximation method. More time steps could be used to increase accuracy at the cost of computational time.

The goal of this study was to determine the effect of a static magnetic field when applied to the system on the induced magnetic dipole moment using the calculated wave function. As the amplitude of the magnetic field increases, the centroid of the orbiting current moved toward the inner tube wall and the positions and magnitudes of the maximum and minimum values of the wave function changed. The induced dipole moments were all negative as expected according to Lenz's law. The dipole moments were found to be a nonlinear function of the magnetic field strength. The nonlinearity observed demonstrates that the bunching of the charged particles near the torus wall may be a method

that could be used to optimize the nonlinear-optical response, and thus enable future applications that rely on the nonlinear-optical response of a material [3].

References

[1] J. E. Houle, "Time-Domain Simulation of the Quantum Magnetic Dipole Moment," Master's Thesis, University of Idaho, Moscow, ID, 2017. [Online]. Available: https://www.lib.uidaho.edu/digital/etd/items/houle_idaho_0089n_11126.html

[2] D. M. Sullivan and D. S. Citrin, "Determination of the eigenfunctions of arbitrary nanostructures using time domain simulation," *Journal of Applied Physics*, vol. 91, no. 5, pp. 3219–3226, Mar. 2002, doi: 10.1063/1.1445277.

[3] M. Riaz, S. K. Earles, A. Kadhim, and A. Azzahrani, "Computer analysis of microcrystalline silicon hetero-junction solar cell with lumerical FDTD/DEVICE," *Int. J. Comp. Mat. Sci. Eng.*, vol. 06, no. 03, p. 1750017, Sep. 2017, doi: 10.1142/S2047684117500178.

[4] D. M. Sullivan, *Electromagnetic Simulation Using the FDTD Method*, Second edition. Hoboken, New Jersey: John Wiley & Sons, Inc., 2013. doi: 10.1002/9781118646700.

[5] D. Sullivan and D. S. Citrin, "Time-domain simulation of two electrons in a quantum dot," *Journal of Applied Physics*, vol. 89, no. 7, pp. 3841–3846, Apr. 2001, doi: 10.1063/1.1352559.

[6] D. M. Sullivan and D. S. Citrin, "Time-domain simulation of quantum spin," *Journal of Applied Physics*, vol. 94, no. 10, pp. 6518–6524, Nov. 2003, doi: 10.1063/1.1618916.

[7] W. Dai, G. Li, R. Nassar, and S. Su, "On the stability of the FDTD method for solving a time-dependent Schrödinger equation," *Numer. Methods Partial Differential Eq.*, vol. 21, no. 6, pp. 1140–1154, Nov. 2005, doi: 10.1002/num.20082.

[8] A. Soriano, E. A. Navarro, J. A. Portí, and V. Such, "Analysis of the finite difference time domain technique to solve the Schrödinger equation for quantum devices," *Journal of Applied Physics*, vol. 95, no. 12, pp. 8011–8018, Jun. 2004, doi: 10.1063/1.1753661.

[9] Q.-Q. Xu and X.-C. Xu, "On the Partial Inverse Problems for the Transmission Eigenvalue Problem of the Schrödinger Operator," *Results Math*, vol. 76, no. 2, p. 79, May 2021, doi: 10.1007/s00025-021-01395-5.

[10] G. B. Ren and J. M. Rorison, "Eigenvalue problem of the Schrödinger equation via the finite-difference time-domain method," *Phys. Rev. E*, vol. 69, no. 3, p. 036705, Mar. 2004, doi: 10.1103/PhysRevE.69.036705.

[11] D. M. Sullivan and P. M. Wilson, "Time-domain determination of transmission in quantum nanostructures," *Journal of Applied Physics*, vol. 112, no. 6, p. 064325, Sep. 2012, doi: 10.1063/1.4754812.

[12] D. M. Sullivan, S. Mossman, and M. G. Kuzyk, "Time-domain simulation of three-dimensional quantum wires," *PLOS ONE*, vol. 11, no. 4, p. e0153802, Apr. 2016, doi: 10.1371/journal.pone.0153802.

[13] D. Sullivan, S. Mossman, and M. G. Kuzyk, "Hybrid quantum systems for enhanced nonlinear optical susceptibilities," *J. Opt. Soc. Am. B*, vol. 33, no. 12, p. E143, Dec. 2016, doi: 10.1364/JOSAB.33.00E143.

[14] D. M. Sullivan and D. S. Citrin, "Determining quantum eigenfunctions in three-dimensional nanoscale structures," *Journal of Applied Physics*, vol. 97, no. 10, p. 104305, May 2005, doi: 10.1063/1.1896437.

[15] D. M. Sullivan, *Quantum Mechanics for Electrical Engineers*. Hoboken, N.J. : Wiley: IEEE Press, 2012.

[16] J.-P. Berenger, "A perfectly matched layer for the absorption of electromagnetic waves," *Journal of Computational Physics*, vol. 114, no. 2, pp. 185–200, Oct. 1994, doi: 10.1006/jcph.1994.1159.

[17] C. Zheng, "A perfectly matched layer approach to the nonlinear Schrödinger wave equations," *Journal of Computational Physics*, vol. 227, no. 1, pp. 537–556, Nov. 2007, doi: 10.1016/j.jcp.2007.08.004.

[18] D. M. Sullivan and D. S. Citrin, "Determination of the eigenfunctions of arbitrary nanostructures using time domain simulation," *Journal of Applied Physics*, vol. 91, no. 5, pp. 3219–3226, Mar. 2002, doi: 10.1063/1.1445277.

[19] D. M. Sullivan and D. S. Citrin, "Determining quantum eigenfunctions in three-dimensional nanoscale structures," *Journal of Applied Physics*, vol. 97, no. 10, p. 104305, May 2005, doi: 10.1063/1.1896437.

[20] A. Zadehgol, "Deterministic Reduced-Order Macromodels for Computing the Broadband Radiation-Field Pattern of Antenna Arrays in FDTD," *IEEE Trans. Antennas Propagat.*, vol. 64, no. 6, pp. 2418–2430, Jun. 2016, doi: 10.1109/TAP.2016.2550052.

[21] A. Zadehgol, "An Impedance Transfer Function Formulation for Reduced-Order Macromodels of Subgridded Regions in FDTD," *IEEE Trans. Antennas Propagat.*, vol. 65, no. 1, pp. 401–404, Jan. 2017, doi: 10.1109/TAP.2016.2627026.

Appendix A – Considerations Implementing FDTD using Python 3.x

Python offers a straight-forward way to implement the Schrödinger equation using the FDTD method. Python packages such as NumPy, SciPy, and Matplotlib allow for easy optimization and visualization of three-dimensional matrices. Using NumPy operations can reduce the number of loops used in the program, thus requiring less computational time to run each simulation. The Numba package provides an easy-to-use function call that speeds up some NumPy functions by converting the top-level Python code into machine code allowing for much quicker calculations. For this thesis, "for" loops were used to perform the FDTD calculations. Optimization techniques such as vectorizing and broadcasting might offer a way to speed up the simulations even more than the Numba package.

The Python package Time lets users efficiently and accurately time certain operations or an entire piece of code. For this thesis, the FDTD, Fourier transform, and magnetic dipole moment calculations were timed using Python. The FDTD calculation took the longest ranging from 63.98 to 115.41 seconds for 10,000 iterations depending on factors such as tube size, time step size, and the state of the system being simulated. The Fourier transform operation ranged from 5.65 to 9.13 seconds and the calculation of the magnetic dipole moment never took more than one second running from 0.23 to 0.61 seconds. Plotting was not accounted for using the Time package. The entire simulation time varied from about two to three minutes per simulation for 10,000 iterations using a computer with an Intel i7-10750H 2.6 GHz processor with 16 GB of RAM.